Position Estimation Based on Sequence Current Decoupling and Reconstruction for PMSM Drives Using Low-Frequency Injection

Yunhao Yan, Guoqiang Zhang, *Senior Member, IEEE*, Gaolin Wang, *Senior Member, IEEE*, Kairan Wang, Binxing Li, *Member, IEEE*, Qiwei Wang, *Member, IEEE*, Dawei Ding, *Member, IEEE*, and Dianguo Xu, *Fellow, IEEE*

***Abstract*—High-frequency (HF) noise is unavoidable with HF injection methods in sensorless permanent magnet synchronous motor (PMSM) drives, limiting its application scenarios. To reduce acoustic noise, a positive-negative sequence current (PNSC) decoupling and reconstruction-based position estimation method using low-frequency (LF) injection is proposed. Based on the positive-negative frequency characteristics of the excited currents, a cross-decoupled complex coefficient filter is used to overcome the phase shift of conventional filters under LF injection. Stability analysis and parameter design demonstrate that the proposed method achieves a phase-shift-free separation between the fundamental and the LF excited currents. Furthermore, to compensate for errors originating from the stator resistance and mutual inductance, a position error suppression method based on the reconstruction of the PNSC is proposed. A unified mapping model between the injection frequency and the estimation error is established to optimize the injection method for increasing estimation accuracy. Analysis of the current power spectral density and A-weighted curve demonstrates that the proposed method can reduce acoustic noise. Finally, the effectiveness of the proposed method is verified on a 2.2-kW interior PMSM drive platform.**

***Index Terms*—Acoustic noise reduction, complex coefficient filter (CCF), current reconstruction, interior permanent magnet synchronous motor (IPMSM), low-frequency rotating injection, sensorless control.**

I. Introduction

With the rapid development of industrial manufacturing, the permanent magnet synchronous motor (PMSM) has become the core power unit due to its high power density and efficiency [1], [2]. An accurate position is critical for achieving high-performance vector control, which is usually obtained through mechanical sensors such as photoelectric encoders and resolvers. However, mechanical sensors carry the risk of failure in harsh conditions such as high temperature, humidity, and vibration. Sensorless control estimates position through algorithms, removing the need for mechanical sensors, and enhancing the reliability in adverse environments [3], [4].

In the medium- and high-speed range, observers are typically designed based on the mathematical model to estimate back electromotive force or flux, and the position is tracked using a phase-locked loop (PLL). Common methods include the sliding mode observer [5], the hybrid active flux observer [6], and the Kalman filter [7]. However, model-based methods may be infeasible during low-speed operation due to their insufficient signal-to-noise ratio (SNR). The high-frequency signal injection (HFSI) method has become the mainstream sensorless control method in the zero- and low-speed regions because it is independent of motor parameters and robust to load disturbances. The HFSI method includes rotating sinusoidal injection [8], pulsating sinusoidal injection [9], and pulsating square-wave injection [10]. To achieve a higher injection frequency, the square-wave injection is usually adopted as an alternative to sinusoidal injection. However, the injection frequency is limited by the inverter switching frequency, which typically lies in the human audible band (20 Hz-20 kHz). Consequently, the injected HF signals generate acoustic noise that limits the applicability of the HFSI method.

Several strategies have been explored to address this issue, including increasing the injection frequency, reducing the injection amplitude, and applying pseudorandom signals. In [11], the injection frequency was raised to the switching frequency, which effectively reduces the noise. However, to ensure sufficient SNR, the injection voltage would be increased accordingly, resulting in lower voltage utilization. Moreover, complete noise removal would require a frequency above 20 kHz, increasing switching losses. Another approach involved reducing the injection amplitude to suppress noise [12]. Yet, this weakens the HF excited currents, degrades the SNR of the position tracking error, and consequently impairs the estimation accuracy. Pseudorandom strategies are widely applied to reduce noise [13], [14], [15], [16]. To mitigate the sharp noise caused by discrete spectral peaks, early work randomized the frequency of two HF voltages, which broadened the excited-current spectrum [13]. In [14], a hybrid injection method combining random frequencies

Received 1 October 2025; revised 1 December 2025; accepted 24 December 2025. Date of publication 30 December 2025; date of current version 20 March 2026. This work was supported by the Research Fund for the National Natural Science Foundation of China under Grant 52522703, Grant 52577041, and Grant 52125701. Recommended for publication by Associate Editor B. Ge. *(Corresponding author: Guoqiang Zhang.)*

The authors are with the School of Electrical Engineering and Automation, Harbin Institute of Technology, Harbin 150001, China (e-mail: 25b306011@stu.hit.edu.cn; zhgq@hit.edu.cn; wgl818@hit.edu.cn; 24b306010@stu.hit.edu.cn; lbx@hit.edu.cn; wqwhit@hit.edu.cn; dingdawei@hit.edu.cn; xudiang@hit.edu.cn).

Color versions of one or more figures in this article are available at https://doi.org/10.1109/TPEL.2025.3649553.

Digital Object Identifier 10.1109/TPEL.2025.3649553

and phases was proposed to reduce noise. To further reduce noise, the pseudorandom HF triangular-wave current signal with random frequencies and phases was injected to eliminate the discrete spectrum for noise suppression [15]. Furthermore, a half-period-switching pseudorandom sinusoidal injection (HPS-PRSI) method spreads the current power spectral density (PSD) and removes discrete harmonics, yielding additional noise reduction. The above methods can effectively reduce noise; however, since the injection frequencies remain relatively high and within the human audible range, the achievable noise reduction is still limited.

Reducing the injection frequency can also decrease noise by shifting the excited current power spectrum from the HF region to the low-frequency (LF) region. However, as the injection frequency decreases, the fundamental and the excited currents become difficult to separate, which may lead to position estimation failure and even instability. To address the separation issue, a model-based current estimator replaced the digital filters and separately evaluated the current containing position information and the feedback current for control [17]. Due to its reliance on the motor model, this method is sensitive to motor parameter variations. Another method estimated the position from the torque disturbances caused by the injected signal [18]. Since the rotor saliency interferes with this method, it is more suitable for surface-mounted PMSM (SPMSM) and relies on accurate motor parameters. To address the impact of filters, an LF pulse voltage injection that separates injection and control periods was introduced [19]. Building on this, a pseudorandom LF pulse voltage injection method was proposed to further reduce noise [20]. However, interrupting the field-oriented control process results in the loss of instantaneous current information and degrades dynamic performance.

For signal injection methods, as the injection frequency decreases, the position estimation errors caused by the stator resistance and filter-induced phase shifts become nonnegligible. The analysis in [21] shows that resistance introduces a dc bias error, degrading the estimation accuracy of rotating injection methods. To compensate for the resistance effect, two sinusoidal signals at different frequencies were injected in the stationary frame, and four equations were used to solve for the position [22]. Nevertheless, the use of two HF signals further increases noise and additional losses. In [23], to mitigate filter effects, the sampled currents and the demodulated signals were passed through a high-pass filter (HPF), and an enhanced PLL with band-pass filter (BPF) characteristics was employed. Nevertheless, when the injection frequency approaches the operating frequency, the phase shift persists. To compensate for the filter-induced phase shifts during demodulation, a dual second-order generalized integrator was employed to suppress the resulting position estimation error [24]. The above methods can reduce the influence of the stator resistance and filters on position estimation; however, problems persist for LF injection.

In this article, a positive-negative sequence current (PNSC) decoupling and reconstruction-based low-frequency injection method is proposed to reduce additional acoustic noise for PMSM drives. To eliminate the position estimation error introduced by conventional filters, a cross-decoupled complex coefficient filter (CD-CCF) based separation method for the fundamental and LF excited currents is developed. Then, a position error suppression scheme based on the reconstruction of the PNSC is proposed. This scheme will compensate for the estimation error caused by the stator resistance and mutual inductance by using both the positive-negative sequence phases. Furthermore, the mapping between the injection frequency and the position estimation error is analyzed to enable frequency optimization for further error reduction. The main innovations of this research are summarized as follows.

1) The LF rotating sinusoidal injection-based sensorless control is proposed to reduce acoustic noise. A unified mapping model between the injection frequency and the position estimation error is established, and the criterion for selecting the optimal injection frequency is clarified.
2) A CD-CCF-based LF excited current extraction method is proposed. The CD-CCF preserves unity gain and zero phase for the target components, avoiding the phase shift introduced by the conventional filtering methods during the separation of the fundamental and LF excited currents.
3) A position estimation error suppression method based on the reconstruction of the PNSC is proposed. By simultaneously utilizing the phase information of the PNSC, the position estimation error resulting from the stator resistance and mutual inductance can be reduced.

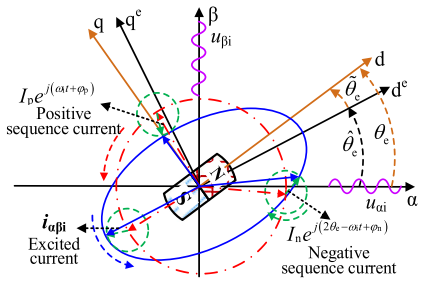

Fig. 1. Reference frames of position sensorless IPMSM drives.

II. Analysis of Position Estimation Error for Low-Frequency Rotating Sinusoidal Injection

The resistance, the mutual inductance, and the filter-induced phase shifts can lead to significant deviations in the estimated position when using low-frequency injection. Fig. 1 shows the reference frames used to analyze the signal injection-based position estimation method for sensorless interior PMSM (IPMSM) drives. The α-β, the d-q, and the d^e-q^e frames denote the stationary frame, the rotary frame, and the estimated frame, respectively. θ_e, $\hat{\theta}_e$, and $\tilde{\theta}_e$ denote the actual position, the estimated position, and the position estimation error, respectively, and $\tilde{\theta}_e = \theta_e - \hat{\theta}_e$.

The LF rotating sinusoidal injection method injects a voltage signal into the α-β axes, with the expression as

$$\begin{bmatrix} u_{\alpha i} \\ u_{\beta i} \end{bmatrix} = U_i \begin{bmatrix} \cos(\omega_i t) \\ \sin(\omega_i t) \end{bmatrix} \tag{1}$$

where $u_{\alpha i}$ and $u_{\beta i}$ are the injected LF voltages in the α-β axes, respectively. U_i and ω_i denote the amplitude and frequency of the LF sinusoidal signal, respectively.

The α-β axis mathematical model, considering the stator resistance and mutual inductance, can be expressed as

$$\begin{bmatrix} u_{\alpha i} \\ u_{\beta i} \end{bmatrix} = \boldsymbol{T}^{-1}(\theta_e) \begin{bmatrix} Z_{dh} & Z_{dqh} \\ Z_{dqh} & Z_{qh} \end{bmatrix} \boldsymbol{T}(\theta_e) \begin{bmatrix} i_{\alpha i} \\ i_{\beta i} \end{bmatrix} \tag{2}$$

where $i_{\alpha i}$ and $i_{\beta i}$ are the α-β axis LF excited currents, respectively. $[Z_{dh}, Z_{dqh}; Z_{qh}, Z_{qdh}] = [R_s+j\omega_i L_{dh}, j\omega_i L_{dqh}; j\omega_i L_{qdh}, R_s+j\omega_i L_{qh}]$ is the d-q axis impedance matrix, where L_{dqh} and L_{qdh} are mutual inductances, and $L_{dqh} = L_{qdh}$. L_{dh} and L_{qh} are the d-q axis self-inductances, respectively. R_s is the stator resistance. j is the imaginary unit.$\boldsymbol{T}(\cdot) = [\cos(\cdot), \sin(\cdot); -\sin(\cdot), \cos(\cdot)]$ is the coordinate transformation matrix.

From (2), the α-β axis LF excited currents can be obtained as

$$\begin{bmatrix} i_{\alpha i} \\ i_{\beta i} \end{bmatrix} = \frac{V_i}{Z_{dh}Z_{qh} - {Z_{dqh}}^2} \cdot \begin{bmatrix} -Z_{dqh}\sin(\omega_i t - 2\theta_e) + Z_0\cos(\omega_i t) - Z_1\cos(\omega_i t - 2\theta_e) \\ Z_1\sin(\omega_i t - 2\theta_e) + Z_0\sin(\omega_i t) - Z_{dqh}\cos(\omega_i t - 2\theta_e) \end{bmatrix} \tag{3}$$

where Z_0 and Z_1 are the average and differential impedances, defined as $Z_0 = (Z_{dh} + Z_{qh})/2$ and $Z_1 = (Z_{dh} - Z_{qh})/2$, respectively.

Substituting the d-q axis impedance matrix into (3) yields the α-β axis LF excited currents, which can be expressed as

$$\begin{bmatrix} i_{\alpha i} \\ i_{\beta i} \end{bmatrix} = I_n \begin{bmatrix} \cos\left(\varphi_n - \omega_i t + 2\theta_e + \frac{\pi}{2}\right) \\ \sin\left(\varphi_n - \omega_i t + 2\theta_e + \frac{\pi}{2}\right) \end{bmatrix} + I_p \begin{bmatrix} \cos\left(\omega_i t - \varphi_p - \frac{\pi}{2}\right) \\ \sin\left(\omega_i t - \varphi_p - \frac{\pi}{2}\right) \end{bmatrix} \tag{4}$$

where I_n and I_p denote the amplitudes of the PNSC, respectively, as given in the following equation:

$$\begin{cases} I_n = \frac{V_i\omega_i\sqrt{(\Gamma L_1 - \chi L_{dqh})^2 + (\chi L_1 + \Gamma L_{dqh})^2}}{\Gamma^2 + \chi^2} \\ I_p = \frac{V_i\sqrt{(-\Gamma\omega_i L_0 + \chi R_s)^2 + (\chi\omega_i L_0 + \Gamma R_s)^2}}{\Gamma^2 + \chi^2} \end{cases}. \tag{5}$$

φ_n and φ_p are the phase angles jointly caused by the resistance and inductance, as given in the following equation:

$$\begin{cases} \varphi_n = \operatorname{atan2}(\Gamma L_1 - \chi L_{dqh}, -\chi L_1 - \Gamma L_{dqh}) - \frac{\pi}{2} \\ \varphi_p = \operatorname{atan2}(-\Gamma\omega_i L_0 + \chi R_s, \chi\omega_i L_0 + \Gamma R_s) - \frac{\pi}{2} \end{cases} \tag{6}$$

where $\Gamma = {R_s}^2 - {\omega_i}^2(L_{dh}L_{qh} - {L_{dqh}}^2)$ and $\chi = \omega_i R_s(L_{dh} + L_{qh})$. L_0 and L_1 denote the average and differential inductances, respectively, which are defined as $L_0 = (L_{dh} + L_{qh})/2$ and $L_1 = (L_{dh} - L_{qh})/2$. atan2(·) denotes the two-argument arctangent.

The conventional method extracts the PNSC in (4) using a synchronous rotating filter and employs a PLL to estimate position [8]. However, due to φ_n, the estimated position exhibits a bias of $-0.5\varphi_n$. Fig. 2 shows the position estimation error under different resistances and injection frequencies. As shown in Fig. 2, the error increases as the injection frequency decreases, and it also increases with larger resistance. Therefore, at reduced injection frequency, the estimation error introduced by the resistance is nonnegligible.

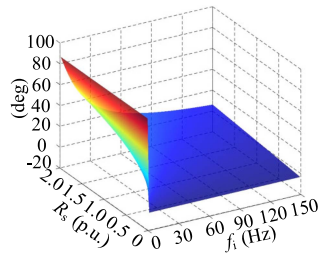

Fig. 2. Position estimation error with different resistances and injection frequencies when considering only resistance and mutual inductance.

On the other hand, the conventional method typically employs a BPF or an HPF to extract the excited currents. Additionally, an HPF is used in the synchronous rotating filter to separate the PNSC. However, at low injection frequency, these filters introduce phase shifts in the extracted excited currents, leading to position estimation errors. The transfer functions of the HPF and BPF are given by

$$\begin{aligned} G_{HP}(s) &= \frac{s^2}{s^2 + (\omega_n/Q)s + {\omega_n}^2}, G_{BP}(s) \\ &= \frac{(\omega_0/Q)s}{s^2 + (\omega_0/Q)s + {\omega_0}^2} \end{aligned} \tag{7}$$

where ω_n is the cutoff frequency of the HPF, ω_0 is the center frequency of the BPF, and Q is the quality factor.

From (7), the phase responses of the BPF and HPF can be obtained as

$$\begin{cases} \angle G_{HP}(j\omega_x) = \pi - \operatorname{atan2}\left(\frac{\omega_x}{Q\omega_n}, 1 - (\omega_x/\omega_n)^2\right) \\ \angle G_{BP}(j\omega_x) = \frac{\pi}{2} - \operatorname{atan2}\left(\frac{\omega_x}{Q\omega_0}, 1 - (\omega_0/Q)^2\right) \end{cases} \tag{8}$$

where ω_x denotes the input-signal frequency.

Fig. 3 shows the magnitude-frequency characteristics of the HPF and BPF for an injection frequency of 80 Hz. As shown in Fig. 3(a), the HPF exhibits significant phase shifts at ω_i and $-\omega_i+2\omega_e$, and its attenuation of the fundamental current is limited. Similarly, Fig. 3(b) shows that when extracting the excited currents at ω_i and $-\omega_i+2\omega_e$, the BPF cannot ensure zero phase shift for both components. Therefore, the conventional HPF or BPF cannot effectively separate the fundamental currents from the LF excited currents.

By jointly accounting for the stator resistance, the mutual inductance, and the filter-induced phase shifts, the position estimation error can be expressed as

$$\tilde{\theta}_e = -\frac{\varphi_n + \angle G_{BP}(j(-\omega_i + 2\omega_e)) + \angle G_{HP}(j(-2\omega_i + 2\omega_e))}{2}. \tag{9}$$

Fig. 4 shows the position estimation error under different resistances and injection frequencies when the phase shifts introduced by using the BPF/HPF are considered. It is observed that the overall error increases as the injection frequency decreases. For the same injection frequency, the error also increases with operating speed.

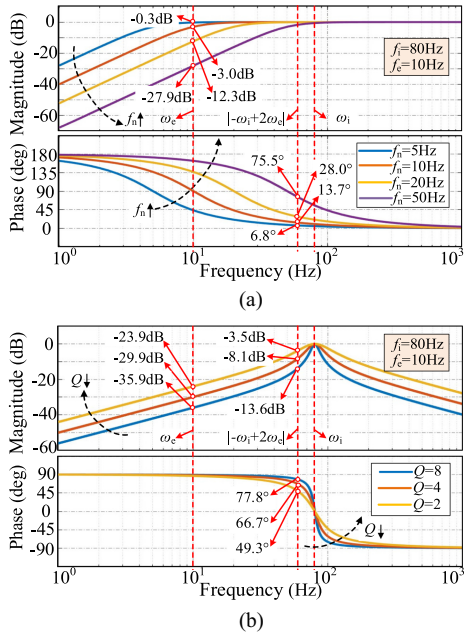

Fig. 3. Amplitude-frequency characteristics of the HPF and BPF in position estimation. (a) Second-order HPF. (b) Second-order BPF.

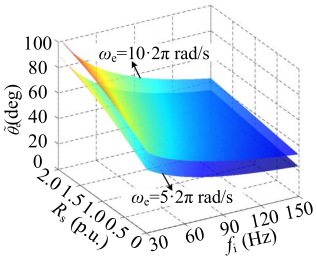

Fig. 4. Position estimation error with different resistances and injection frequencies when considering resistance, mutual inductance, and filter-induced phase shifts.

III. Proposed LF Injection Method Based on the PNSC Decoupling and Reconstruction

To achieve accurate position estimation at low injection frequency, a LF rotating sinusoidal injection method based on the PNSC decoupling and reconstruction is proposed. The control block diagram is shown in Fig. 5. Leveraging the CCF's ability to separate positive-negative frequency harmonics, this method can effectively separate the fundamental currents from the LF excited currents. Moreover, to address the position estimation error caused by the stator resistance and mutual inductance, a PNSC reconstruction-based demodulation is developed.

A. PNSC Decoupling and Reconstruction-Based Position Estimation Method

Based on the frequency characteristics of the PNSC, a CCF is employed to extract the LF excited currents, as shown in the CD-CCF block in Fig. 5. This filter separates the components at ω_i and $-\omega_i+2\omega_e$, and simultaneously isolates the fundamental current at ω_e. Its transfer function can be expressed as

$$\begin{cases} G_0(s) = \frac{i_{\alpha\beta f}(s)}{i_{\alpha\beta}(s)} = \frac{k}{s-j\omega_e+k} \\ G_1(s) = \frac{i_{\alpha\beta i1}(s)}{i_{\alpha\beta}(s)} = \frac{k}{s-j(-\omega_i+2\omega_e)+k} \\ G_2(s) = \frac{i_{\alpha\beta i2}(s)}{i_{\alpha\beta}(s)} = \frac{k}{s-j\omega_i+k} \end{cases} \tag{10}$$

where $i_{\alpha\beta f}$, $i_{\alpha\beta i1}$, and $i_{\alpha\beta i2}$ are the fundamental currents, the negative sequence excited currents, and the positive sequence excited currents in the α-β axes, respectively. k is the gain of the CD-CCF.

To enhance the performance of signal extraction, a cross-decoupling network is designed, which can be expressed as

$$\begin{cases} i_{\alpha\beta f}(s) = G_0(s)\left(i_{\alpha\beta}(s) - i_{\alpha\beta i1}(s) - i_{\alpha\beta i2}(s)\right) \\ i_{\alpha\beta i1}(s) = G_1(s)\left(i_{\alpha\beta}(s) - i_{\alpha\beta f}(s) - i_{\alpha\beta i2}(s)\right) \\ i_{\alpha\beta i2}(s) = G_2(s)\left(i_{\alpha\beta}(s) - i_{\alpha\beta f}(s) - i_{\alpha\beta i1}(s)\right) \end{cases}. \tag{11}$$

According to (11), the transfer function between the extracted currents and the sampled currents can be expressed as

$$\begin{aligned} G_H(s) &= \frac{i_{\alpha\beta i}(s)}{i_{\alpha\beta}(s)} = \frac{i_{\alpha\beta i1}(s) + i_{\alpha\beta i2}(s)}{i_{\alpha\beta}(s)} \\ &= \frac{\left(1-G_0(s)\right)\left({G_1}^{-1}(s) + {G_2}^{-1}(s) - 2\right)}{\left({G_1}^{-1}(s) - G_0(s)\right)\left({G_2}^{-1}(s) - 1\right) + \left(1-G_0(s)\right)\left({G_1}^{-1}(s) - 1\right)}. \end{aligned} \tag{12}$$

From (10) and (12), $G_H(s)$ can be derived as

$$G_H(s) = \frac{2k\left(s^2 - 2j\omega_e s - {\omega_e}^2\right)}{s^3 + (3k - 3j\omega_e)s^2 + p_1 s + p_2} \tag{13}$$

where

$$\begin{cases} p_1 = {\omega_i}^2 - 2\omega_e\omega_i - 2{\omega_e}^2 - 6j\omega_e k \\ p_2 = {\omega_i}^2 k - 2\omega_e\omega_i k - 2{\omega_e}^2 k - j\omega_e{\omega_i}^2 + 2j{\omega_e}^2\omega_i \end{cases}. \tag{14}$$

Fig. 6 shows the Bode diagram of the proposed CD-CCF for extracting the LF excited currents, with the injection frequency set to 80 Hz. The Bode diagram is calculated and plotted based on the closed-loop transfer function derived analytically from the block diagram. As observed, the filter extracts the excited currents at ω_i and $-\omega_i+2\omega_e$ without phase shift or magnitude attenuation, while strongly suppressing the fundamental component at ω_e. Therefore, the proposed CD-CCF can effectively separate the fundamental currents from the excited currents.

Also, conventional demodulation relies on the negative-sequence current, and thus, the stator resistance will introduce a position estimation error that increases as the injection frequency decreases. Fig. 7 shows the phase variation of the PNSC with different resistances and injection frequencies, which is plotted according to (6) from the analytical derivation. Since the expression of phase shift in (6) does not contain a voltage amplitude term, the injection voltage amplitude does not induce any phase variations. The accurate extraction of the excited currents is critical for ensuring position estimation performance. However, if the injection amplitude is too low, it will be difficult to extract accurate LF excited current information. The higher the injection amplitude, the higher the SNR, but also the higher the torque ripples and the lower the available voltage margin. Therefore,

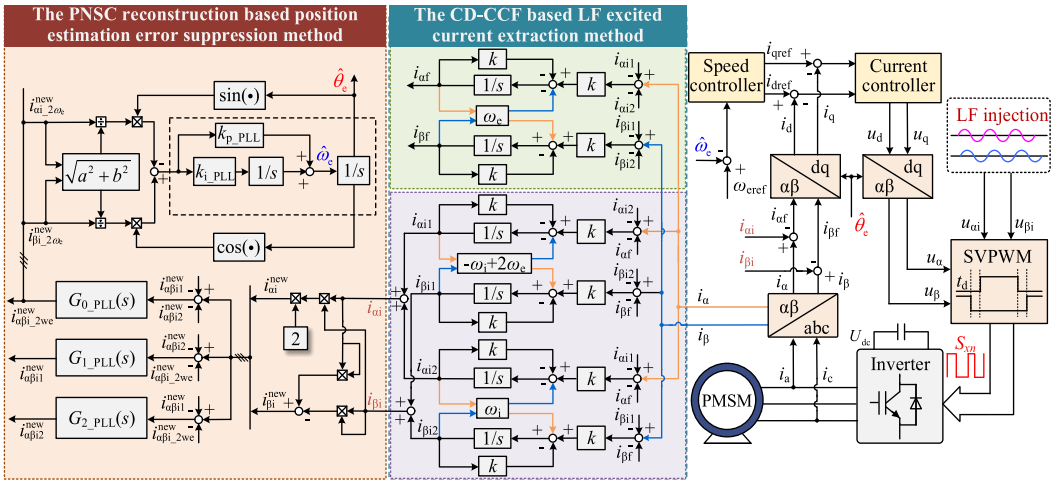

Fig. 5. Block diagram of the proposed PNSC decoupling and reconstruction-based position estimation method.

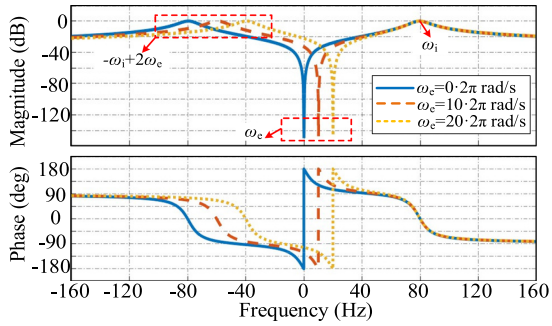

Fig. 6. Bode diagram of the CD-CCF for LF excited current extraction.

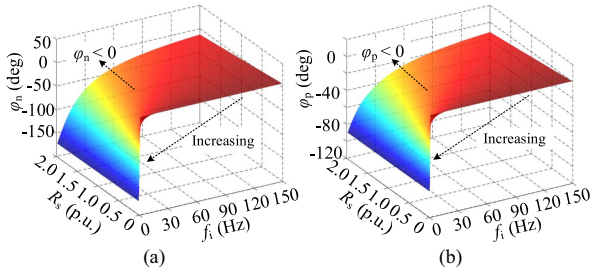

Fig. 7. Phase variation of the PNSC with different resistances and injection frequencies. (a) Negative-sequence current phase. (b) Positive-sequence current phase.

the injection voltage amplitude is typically selected such that the excited current magnitude falls between 5% and 20% of the rated current. And then, as shown in Fig. 7, since the phases of the PNSC share the same sign, a PNSC reconstruction-based error suppression method is proposed. This method employs the positive-sequence phase to compensate for the error induced by the negative-sequence phase. The reconstructed excited currents are given in the following equations:

$$\begin{aligned} i_{\beta\mathrm{i}}^{\mathrm{new}} &= 2i_{\alpha\mathrm{i}}i_{\beta\mathrm{i}} \\ &= -{I_{\mathrm{n}}}^2\sin\left(-2\omega_{\mathrm{i}}t+2\varphi_{\mathrm{n}}+4\theta_{\mathrm{e}}+2\varphi_{\mathrm{d}}\right) \\ &\quad -{I_{\mathrm{p}}}^2\sin\left(2\omega_{\mathrm{i}}t-2\varphi_{\mathrm{p}}-2\varphi_{\mathrm{d}}\right)+2I_{\mathrm{p}}I_{\mathrm{n}}\sin\left(\varphi_{\mathrm{n}}-\varphi_{\mathrm{p}}+2\theta_{\mathrm{e}}\right) \end{aligned} \tag{15}$$

$$\begin{aligned} i_{\alpha\mathrm{i}}^{\mathrm{new}} &= {i_{\alpha\mathrm{i}}}^2-{i_{\beta\mathrm{i}}}^2 \\ &= -{I_{\mathrm{n}}}^2\cos\left(-2\omega_{\mathrm{i}}t+2\varphi_{\mathrm{n}}+4\theta_{\mathrm{e}}+2\varphi_{\mathrm{d}}\right) \\ &\quad -{I_{\mathrm{p}}}^2\cos\left(2\omega_{\mathrm{i}}t-2\varphi_{\mathrm{p}}-2\varphi_{\mathrm{d}}\right)+2I_{\mathrm{p}}I_{\mathrm{n}}\cos\left(\varphi_{\mathrm{n}}-\varphi_{\mathrm{p}}+2\theta_{\mathrm{e}}\right) \end{aligned} \tag{16}$$

where φ_{d} denotes the phase angle introduced by system delays, including PWM-update and hardware delays.

From (15) and (16), the reconstructed currents contain the $2\omega_{\mathrm{e}}$, $2\omega_{\mathrm{i}}$, and -2(ω_{i}-2ω_{e}) components. Only the $2\omega_{\mathrm{e}}$ component is used for position estimation. Moreover, the spectral distribution of the reconstructed currents resembles that of the sampled currents. Therefore, a CD-CCF-based PLL (CD-CCF-PLL) is designed to extract the required component for position estimation, which can be expressed as

$$\begin{cases} G_{0\_\mathrm{PLL}}(s)=\dfrac{i_{\alpha\beta\mathrm{i}\_2\omega_{\mathrm{e}}}^{\mathrm{new}}(s)}{i_{\alpha\beta\mathrm{i}}^{\mathrm{new}}(s)}=\dfrac{k_1}{s-j2\omega_{\mathrm{e}}+k_1} \\ G_{1\_\mathrm{PLL}}(s)=\dfrac{i_{\alpha\beta\mathrm{i}1}^{\mathrm{new}}(s)}{i_{\alpha\beta\mathrm{i}}^{\mathrm{new}}(s)}=\dfrac{k_1}{s-j(-2\omega_{\mathrm{i}}+4\omega_{\mathrm{e}})+k_1} \\ G_{2\_\mathrm{PLL}}(s)=\dfrac{i_{\alpha\beta\mathrm{i}2}^{\mathrm{new}}(s)}{i_{\alpha\beta\mathrm{i}}^{\mathrm{new}}(s)}=\dfrac{k_1}{s-j2\omega_{\mathrm{i}}+k_1} \end{cases}. \tag{17}$$

where $i_{\alpha\beta\mathrm{i}\_2\omega_{\mathrm{e}}}^{\mathrm{new}}$, $i_{\alpha\beta\mathrm{i}1}^{\mathrm{new}}$, and $i_{\alpha\beta\mathrm{i}2}^{\mathrm{new}}$ are the fundamental components, the negative sequence components, and the positive sequence components of the α-β axis reconstructed excited currents, respectively. k_1 is the gain of the CD-CCF-PLL.

For the designed CD-CCF-PLL, the transfer function between the $2\omega_{\mathrm{e}}$ component and the reconstructed currents is given in (24). Combining (17) and (24), shown at the bottom of the next page, the simplified transfer function $G_{\mathrm{H\cdot PLL}}(s)$ can be obtained as (25), shown at the bottom of the next page.

Fig. 8 shows the Bode diagram of the proposed CD-CCF-PLL with the injection frequency set to 80 Hz. As observed, the filter extracts the $2\omega_{\mathrm{e}}$ component for position estimation without phase shift or magnitude attenuation, while strongly suppressing the components at $2\omega_{\mathrm{i}}$ and 2(-ω_{i}+2ω_{e}).

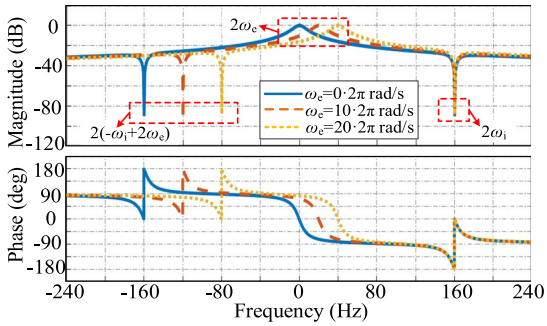

Fig. 8. Bode diagram of the CD-CCF-PLL for $2\omega_e$ current component extraction.

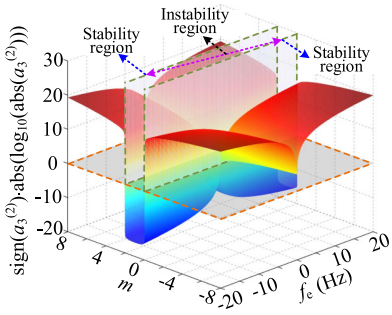

Fig. 9. Influence of coefficient m on the stability of the CD-CCF.

After eliminating the $2\omega_i$ and $-2(\omega_i-2\omega_e)$ components from the reconstructed currents using (17), the equivalent position tracking error obtained via the heterodyning method is

$$\varepsilon = \frac{i^{new}_{\beta i\_2\omega_e}\cos\left(2\hat{\theta}_e\right) - i^{new}_{\alpha i\_2\omega_e}\sin\left(2\hat{\theta}_e\right)}{\sqrt{\left(i^{new}_{\alpha i\_2\omega_e}\right)^2 + \left(i^{new}_{\beta i\_2\omega_e}\right)^2}} = \sin\left(\varphi_n - \varphi_p + 2\tilde{\theta}_e\right). \tag{18}$$

Finally, feeding the signal in (18) into the PLL enables position estimation, thereby achieving sensorless control at low injection frequency.

B. Stability Analysis and Parameter Design

To ensure stable operation, the stability should be analyzed. Firstly, the influence of parameters on the stability of fundamental current and LF excited current extraction is examined. The characteristic polynomial of $G_H(s)$ is

$$\lambda(s) = s^3 + (3k - 3j\omega_e)s^2 + p_1 s + p_2. \tag{19}$$

Following the research presented I [25], the generalized Routh matrix can be obtained from (19), with the relevant parameters given by

$$\begin{cases} a_0 = 1, a_1 = 3k, a_2 = {\omega_i}^2 - 2\omega_e\omega_i - 2{\omega_e}^2, \\ a_3 = {\omega_i}^2 k - 2\omega_e\omega_i k - 2{\omega_e}^2 k \\ b_1 = -6\omega_e, b_2 = -6\omega_e k, b_3 = 2{\omega_e}^2\omega_i - \omega_e{\omega_i}^2 \\ {b_1}^{(1)} = a_1 b_1 - a_0 b_2, {a_2}^{(1)} = a_1 a_2 - a_0 a_3, {b_3}^{(1)} = a_1 b_3 \\ {a_2}^{(2)} = a_1 {a_2}^{(1)} + {b_1}^{(1)} b_2, {b_3}^{(2)} = a_1 {b_3}^{(1)} - {b_1}^{(1)} a_3 \\ {b_2}^{(1)} = {a_2}^{(2)} b_2 - a_1 {b_3}^{(2)}, {a_3}^{(1)} = {a_2}^{(2)} a_3 \\ {a_3}^{(2)} = {a_2}^{(2)} {a_3}^{(1)} + {b_2}^{(1)} {b_3}^{(2)} \end{cases}. \tag{20}$$

According to the generalized Routh criterion, the stability condition for $G_H(s)$ is

$$a_0 > 0, a_1 > 0, {a_2}^{(2)} > 0, {a_3}^{(2)} > 0. \tag{21}$$

Therefore, from (20) and (21), the designed CD-CCF is stable when the gain k and injection frequency ω_i satisfy (22). Here, m denotes the proportional factor, whose admissible range is shown in Fig. 9.

$$k > 0, \omega_i > m\omega_e. \tag{22}$$

Fig. 9 is designed to visualize the stable region (${a_3}^{(2)} > 0$) for different m and ω_e. Since the value of ${a_3}^{(2)}$ varies significantly with both m and ω_e, a logarithmic expression is adopted; consequently, sign(${a_3}^{(2)}$)·abs(log$_{10}$(abs(${a_3}^{(2)}$))) is employed to provide a more intuitive representation regarding the influence of coefficient m on the stability of the CD-CCF.

Similarly, analysis yields the admissible parameter range of the CD-CCF-PLL during the PNSC reconstruction as

$$k_1 > 0, \omega_i > m\omega_e \tag{23}$$

where m has the same admissible range as in (22).

To further evaluate the influence of gain k on the CD-CCF for LF excited current extraction, the Bode diagram for different k is shown in Fig. 10(a). As gain k increases, the CD-CCF responds faster but with lower extraction accuracy. Fig. 10(b) shows the Bode diagram of the CD-CCF-PLL for different gains k_1. A larger k_1 similarly yields faster response but lower accuracy. Hence, the parameter selection requires a tradeoff between response speed and extraction accuracy.

On the other hand, although the PNSC reconstruction-based method reduces the estimation error, a residual error of $0.5(\varphi_p\text{-}\varphi_n)$ remains in the estimated position. Therefore,

$$G_{H\_PLL}(s) = \frac{i_{\alpha\beta i\_2\omega_e}(s)}{i^{new}_{\alpha\beta i}(s)} = \frac{\left({G_{1\_PLL}}^{-1}(s) - 1\right)\left({G_{2\_PLL}}^{-1}(s) - 1\right)}{{G_{0\_PLL}}^{-1}(s)\left({G_{1\_PLL}}^{-1}(s) - 1\right)\left({G_{2\_PLL}}^{-1}(s) - 1\right) + \left({G_{0\_PLL}}^{-1}(s) - 1\right)\left({G_{1\_PLL}}^{-1}(s) + {G_{2\_PLL}}^{-1}(s) - 2\right)} \tag{24}$$

$$G_{H\_PLL}(s) = \frac{k_1\left(s^2 - 4j\omega_e s + 4{\omega_i}^2 - 8\omega_e\omega_i\right)}{s^3 + (3k_1 - 6j\omega_e)s^2 + (4{\omega_i}^2 - 8{\omega_e}^2 - 8\omega_e\omega_i - 12j\omega_e k_1)s + 8j\omega_e\omega_i(-\omega_i + 2\omega_e) - 4k_1(\omega_i(-\omega_i + 2\omega_e) + 2{\omega_e}^2)}. \tag{25}$$

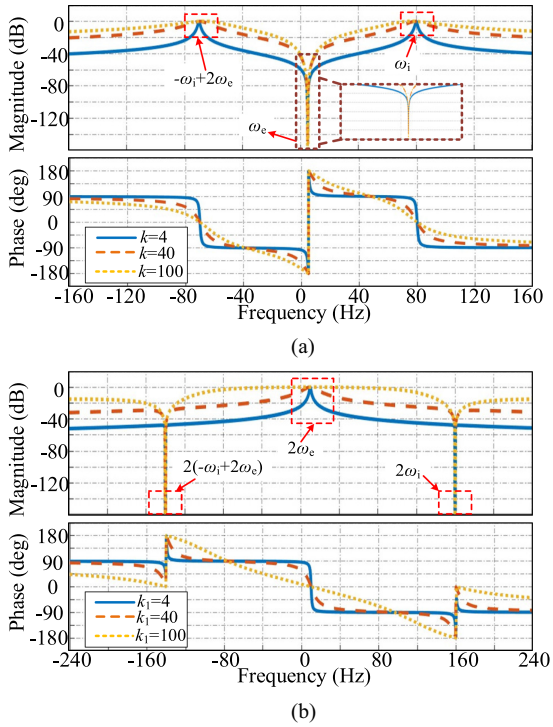

Fig. 10. Bode diagram with different gains. (a) CD-CCF. (b) CD-CCF-PLL.

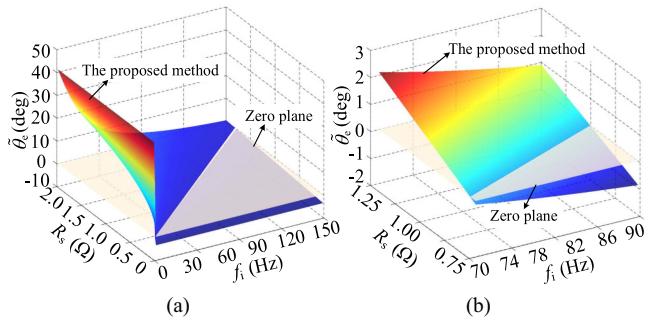

Fig. 11. Position estimation error of the proposed method with different resistances and injection frequencies. (a) f_i = (0, 150 Hz), R_s = (0, 2.0 p.u.). (b) f_i = (70, 90 Hz), R_s = (0.75, 1.25 p.u.).

a systematic mapping between the position error and the resistance and injection frequency is required for this demodulation scheme. Fig. 11 shows the position error versus the resistance and injection frequency. Fig. 11(a) considers an injection frequency range of (0, 150 Hz) and a resistance range of (0, 2p.u.). The results show that the proposed demodulation significantly reduces the position error relative to the conventional method. However, at very low injection frequency, a nonnegligible error persists. Hence, the injection frequency should be selected to maintain high accuracy while enabling LF injection. Fig. 11(b) considers an injection frequency range of (70, 90 Hz) and a resistance range of (0.75, 1.25p.u.). Within this range, the position error remains within (-2°, 3°). Accordingly, 80 Hz is selected as the injection frequency. It is also noted that the position error at this operating point includes contributions from both the resistance and the mutual inductance, so no additional compensation for the mutual inductance is required.

The selection of the injection frequency should take into account the position estimation error caused jointly by the injection frequency, the inductance, and the stator resistance, as well as the stability of the CD-CCF. Subsequently, the principle for selecting the injection frequency can be expressed as

$$\begin{cases} \boldsymbol{O}(q,n) = \boldsymbol{K}(q) \cap \mathbf{M}(n) \\ \boldsymbol{K} = \left\{ q \in S \middle| \varphi_{\mathrm{p}}(q) - \varphi_{\mathrm{n}}(q) \le 2\tilde{\theta}_{\mathrm{e\_max}} \right\} \\ \mathbf{M} = \left\{ n \in S \middle| a_1 > 0, a_2{}^{(2)} > 0, a_3{}^{(2)} > 0 \right\} \\ q = (\omega_{\mathrm{i}}, R_{\mathrm{s}}, L_{\mathrm{dqh}}, L_{\mathrm{dh}}, L_{\mathrm{qh}}) \\ n = (\omega_{\mathrm{i}}, \omega_{\mathrm{e}}, k) \end{cases} \tag{26}$$

where $\boldsymbol{O}(q, n)$ is the expected set of the injection frequency when considering both the position estimation error and the stability. $\tilde{\theta}_{\mathrm{e\_max}}$ is the expected maximum position estimation error.

C. Analysis of A-Weighted Noise Characteristics

The PSD is used to analyze the noise distribution of the HF injection method [13], [14], [15], [16]. For a fixed-frequency sinusoidal injection, the HF current PSD can be expressed as

$$S(f) = \frac{1}{{T_{\mathrm{inj}}}^2} |I_{\mathrm{inj}}(f)|^2 \delta(f - f_{\mathrm{inj}}) \tag{27}$$

where T_{inj} is the period of the HF signal. f_{inj} is the injection frequency. $I_{\mathrm{inj}}(f)$ denotes the Fourier transform of the excited current. $\delta(\cdot)$ denotes the unit impulse function.

Based on the excited currents under rotating injection, the current PSD can be expressed as

$$S_{\mathrm{R}}(f) = {f_{\mathrm{n}}}^2 |I_{\mathrm{n}}(f)|^2 \delta(f - f_{\mathrm{n}}) + {f_{\mathrm{p}}}^2 |I_{\mathrm{p}}(f)|^2 \delta(f - f_{\mathrm{p}}) \tag{28}$$

where f_{n} and f_{p} are the frequencies of the PNSC, respectively, given by $f_{\mathrm{n}} = -f_{\mathrm{i}} + 2f_{\mathrm{e}}$ and $f_{\mathrm{p}} = f_{\mathrm{i}}$. f_{i} is the injection frequency, and f_{e} is the electrical operating frequency. $I_{\mathrm{n}}(f)$ and $I_{\mathrm{p}}(f)$ denote the Fourier transforms of the PNSC, respectively.

From (28), the fixed-frequency sinusoidal injection (FFSI) produces prominent phase current PSD peaks at f_{n} and f_{p}, which are tied to the operating and injection frequencies. The current PSD reflects the noise, so the noise frequencies coincide with these peaks. As the injection frequency increases, the noise shifts to higher frequencies. As the amplitude-to-frequency ratio of the injected signal increases, the noise level rises.

Acoustic noise results from the combined contribution of multiple frequency components. Human hearing exhibits nonuniform sensitivity over frequency, which can be quantified by the A-weighted curve. The A-weighted curve is widely used in environmental noise measurement, hearing protection assessment, and industrial noise certification [26], which is

$$\begin{cases} R_{\mathrm{a}}(f) = \frac{12200^2 \cdot f^4}{M} \\ M = \left(f^2 + 20.6^2\right)\left(f^2 + 12200^2\right)\left(f^2 + 107.7^2\right)^{0.5} \\ \left(f^2 + 737.9^2\right)^{0.5} \\ L_{\mathrm{A}} = 2.0 + 20\log\left(R_{\mathrm{a}}(f)\right) \end{cases} \tag{29}$$

where L_{A} is the weighting factor computed from the A-weighted formula.

Fig. 12 shows the frequency response of the A-weighted filter computed from (29). The curve peaks at 1-5 kHz, indicating

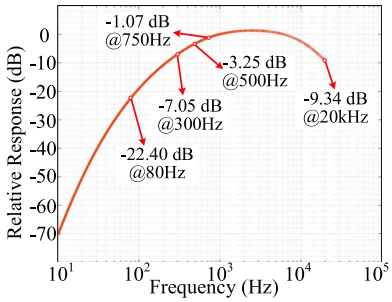

Fig. 12. Frequency response of A-weighted filter.

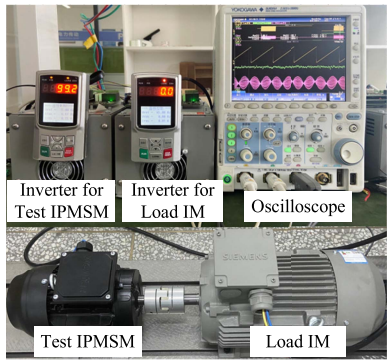

Fig. 13. 2.2-kW IPMSM experimental platform.

higher auditory sensitivity to mid frequencies than to low or high frequencies. The A-weighted sound level is computed as

$$L_{\mathrm{A-Weightd}} = L_f + L_{\mathrm{A}} \tag{30}$$

where $L_{\mathrm{A\text{-}Weighted}}$ is the A-weighted sound level in dBA, and L_f is the actual noise level in dB.

Therefore, increasing or decreasing the injection frequency can suppress noise. However, increasing the frequency is limited by drive capability, and excessively high values raise converter losses and reduce voltage utilization. The LF injection adopted in this article reduces acoustic noise and mitigates penalties on converter loss and voltage utilization.

D. Analysis of Inverter Nonlinearity

The dead-time effect is an important factor of inverter nonlinearity, which is unavoidable at low speeds, posing a major challenge to sensorless control of PMSM. The impact of the inverter nonlinearity on the proposed method primarily manifests as the introduction of harmonics in the estimated position.

When considering the inverter nonlinearity, the α-β axis LF excited currents can be expressed as (31) shown at the bottom of this page, where $I_{\alpha\mathrm{hn6k}}$, $I_{\beta\mathrm{hn6k}}$, $\varphi_{\alpha\mathrm{hn6k}}$, and $\varphi_{\beta\mathrm{hn6k}}$ are the magnitude and phase components of the 6kth harmonic components for the negative sequence current in the α-β axes, respectively. $I_{\alpha\mathrm{hp6k}}$, $I_{\beta\mathrm{hp6k}}$, $\varphi_{\alpha\mathrm{hp6k}}$, and $\varphi_{\beta\mathrm{hp6k}}$ are the magnitude and phase components of the 6kth harmonic components for the positive sequence current in the α-β axes, respectively.

According to (31), the inverter nonlinearity introduces additional harmonics into the LF excited currents, consequently causing fluctuations in the estimated position.

IV. Experimental Results

Fig. 13 shows the 2.2-kW IPMSM experimental platform, and the motor parameters are listed in Table I. An ARM chip STM32F103VCT6, with a clock frequency of 72 MHz, is applied to execute the entire sensorless control algorithm. The PWM carrier frequency, the sampling frequency, and the control frequency are set to 6 kHz. The test IPMSM is coaxially coupled to a load induction motor (IM), and the load torque is provided by the coaxially connected IM. An incremental encoder with 2000 p/r is applied to detect the actual rotor position for comparison only. Acoustic measurements use a commercial sound level meter (BSWA 308). For the proposed method, the injection frequency is 80 Hz, and the injection amplitude is 9 V. To optimize the position estimation performance of the proposed method, dead-time compensation is used in the experiments.

TABLE I
Parameters of the Test IPMSM

Parameter	Value	Parameter	Value
Rated power	2.2 kW	Phase resistance	1.86 Ω
Rated voltage	380 V	D-axis inductance	22 mH
Rated current	4.4 A	Q-axis inductance	51 mH
Rated speed	1500 r/min	Pairs of poles	3
Rated torque	14 N·m	Magnetic flux	0.46 Wb
DC voltage	537 V	Peak of back-EMF	146 V @1000 r/min

Fig. 14 shows the extracted α-axis fundamental current and LF excited current using the CD-CCF at 100 r/min under rated load. From the FFT result in Fig. 14(b), the extracted α-axis LF current contains 70 Hz (f_{i} - 2f_{e}) and 80 Hz (f_{i}) components, corresponding to the PNSC, respectively. The negative-sequence and positive-sequence current amplitudes are 0.18 A and 0.57 A, respectively, and the 5 Hz (f_{e}) fundamental component is almost completely removed. From the FFT result in Fig. 14(c), the extracted α-axis fundamental current has a 5 Hz (f_{e}) amplitude of 6.41 A, and the 70 Hz (f_{i} - 2f_{e}) and 80 Hz (f_{i}) components are also removed. These results confirm that the proposed CD-CCF

$$\begin{cases} {i_{\alpha\mathrm{i}}}' = \\ \quad \cos\left(\varphi_{\mathrm{n}} - \omega_{\mathrm{i}}t + 2\theta_{\mathrm{e}} + \frac{\pi}{2}\right)\left\{I_{\mathrm{n}} + \sum_{k=1} I_{\alpha\mathrm{hn6k}} \cos\left(6k\hat{\omega}_{\mathrm{e}}t + \varphi_{\alpha\mathrm{hn6k}}\right)\right\} \\ \quad + \cos\left(\omega_{\mathrm{i}}t - \varphi_{\mathrm{p}} - \frac{\pi}{2}\right)\left\{I_{\mathrm{p}} + \sum_{k=1} I_{\alpha\mathrm{hp6k}} \cos\left(6k\hat{\omega}_{\mathrm{e}}t + \varphi_{\alpha\mathrm{hp6k}}\right)\right\} \\ {i_{\beta\mathrm{i}}}' = \\ \quad \sin\left(\varphi_{\mathrm{n}} - \omega_{\mathrm{i}}t + 2\theta_{\mathrm{e}} + \frac{\pi}{2}\right)\left\{I_{\mathrm{n}} + \sum_{k=1} I_{\beta\mathrm{hn6k}} \sin\left(6k\hat{\omega}_{\mathrm{e}}t + \varphi_{\beta\mathrm{hn6k}}\right)\right\} \\ \quad + \sin\left(\omega_{\mathrm{i}}t - \varphi_{\mathrm{p}} - \frac{\pi}{2}\right)\left\{I_{\mathrm{p}} + \sum_{k=1} I_{\beta\mathrm{hp6k}} \sin\left(6k\hat{\omega}_{\mathrm{e}}t + \varphi_{\beta\mathrm{hp6k}}\right)\right\} \end{cases} . \tag{31}$$

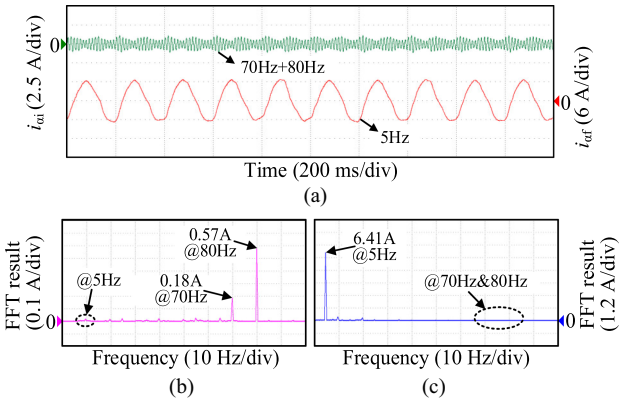

Fig. 14. Experimental results of the extracted α-axis fundamental current and LF excited current. (a) Current waveforms. (b) FFT result of the α-axis LF excited current. (c) FFT result of the α-axis fundamental current.

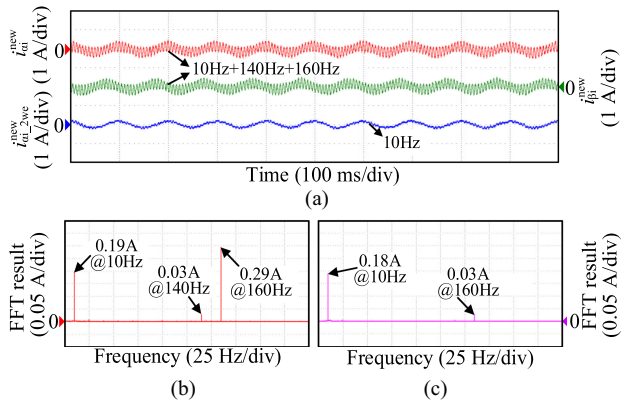

Fig. 15. Experimental results of the reconstructed LF excited currents. (a) Current waveforms. (b) FFT result of the α-axis reconstructed current. (c) FFT result of the extracted $2f_e$ component in the α-axis reconstructed current.

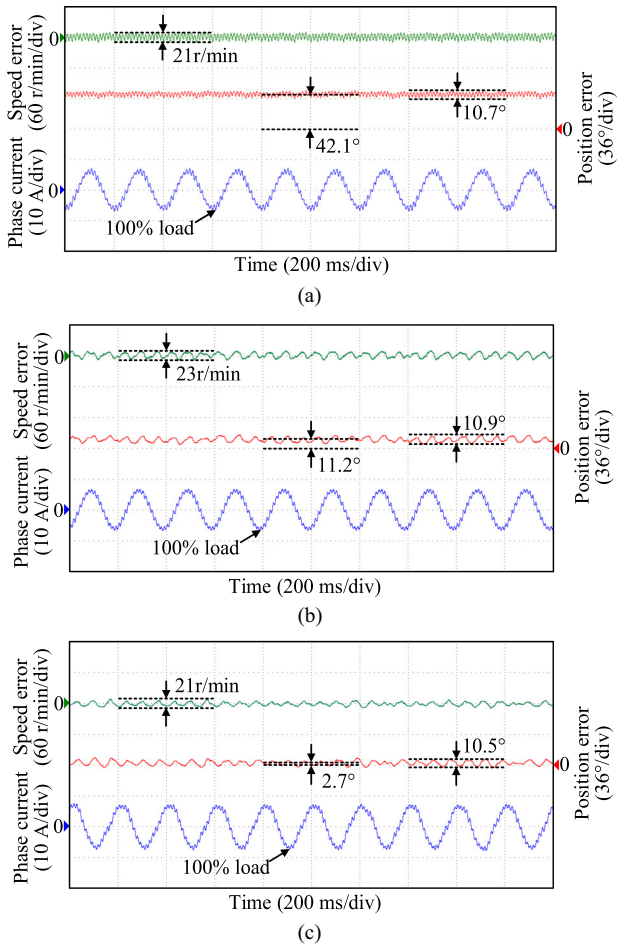

Fig. 16. Experimental results at 100 r/min under rated load. (a) Conventional BPF/HPF method in sensored control. (b) CD-CCF-based method in sensorless control. (c) Proposed method in sensorless control.

can effectively separate the fundamental currents from the LF excited currents.

Fig. 15 shows the reconstructed currents and the $2f_e$ component extracted by the CD-CCF-PLL at 100 r/min under rated load. From the FFT result in Fig. 15(b), the reconstructed α-axis LF current contains 10 Hz ($2f_e$), 140 Hz ($2f_i$ - $4f_e$), and 160 Hz ($2f_i$) components. The 10 Hz ($2f_e$) component is used for position estimation, and the 140 Hz ($2f_i$ - $4f_e$) and 160 Hz ($2f_i$) components should be suppressed. Fig. 15(c) shows the FFT result of the extracted $2\omega_e$ component, in which the 10 Hz ($2f_e$) amplitude is 0.18 A, and the 160 Hz ($2f_i$) component decreases from 0.29 A to 0.03 A, and the 140 Hz ($2f_i$ - $4f_e$) component is almost eliminated. These results confirm that the proposed CD-CCF-PLL can effectively extract the current component for position estimation from the reconstructed currents.

Fig. 16 shows the experimental results at 100 r/min under rated load for different methods. Fig. 16(a) shows the result of the conventional BPF/HPF method in sensored control. The BPF separates the fundamental and excited currents with a 30 Hz bandwidth. The HPF separates the PNSC with a 50 Hz cutoff. Due to the stator resistance and filter-induced phase shifts, the position error reaches 42.1°, which prevents sensorless operation. Fig. 16(b) shows the result of the CD-CCF in sensorless control. The CD-CCF is used to separate the fundamental and LF excited currents, and the negative-sequence component is used for position estimation. The phase shift introduced by conventional filters is reduced, yet the resistance produces an error of about 11.2°. This error is lower than with the conventional method, which verifies the effectiveness of the CD-CCF. Fig. 16(c) shows the results of the CD-CCF combined with the PNSC reconstruction in sensorless control. This method mitigates the effects of the stator resistance and filter phase shift at low injection frequency, and the position error decreases to about 2.7°.

Fig. 17 shows the experimental results with different injection amplitudes and frequencies under rated load. For Fig. 17(a), the injection frequency is set as 60 Hz, and the position estimation error reaches 5.8°, which is larger than the error at 80 Hz. This occurs because lower injection frequencies increase the influence of the stator resistance on position estimation. For Fig. 17(b), with the injection frequency maintained at 80 Hz and the amplitude increased to 16 V, the peak-to-peak position estimation error is reduced to 5.4°. This improvement is attributed to the higher SNR achieved with greater injection voltage. However, as visible from the phase currents, the ripple

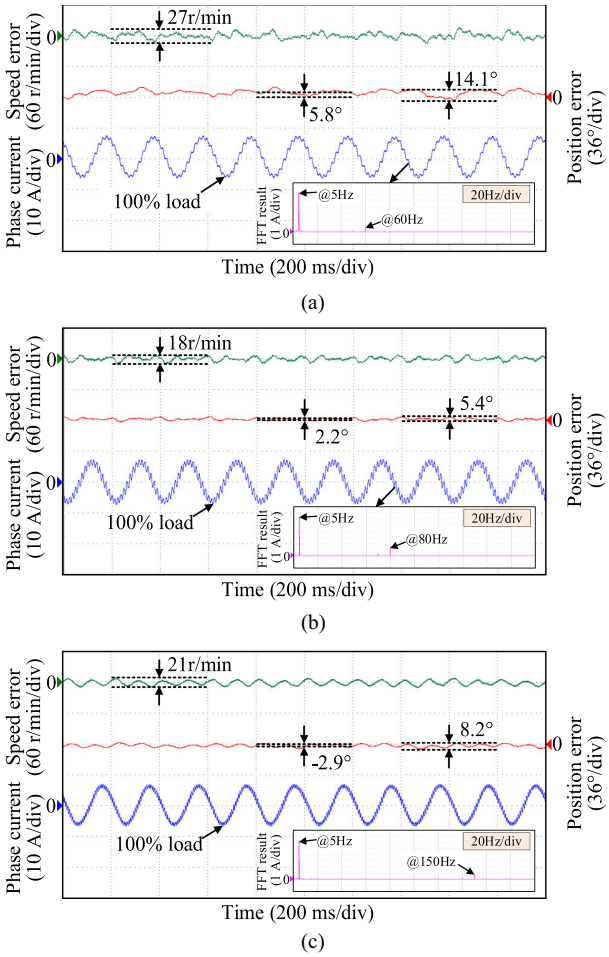

Fig. 17. Experimental results under different injection amplitudes and frequencies. (a) 60 Hz, 6 V. (b) 80 Hz, 16 V. (c) 150 Hz, 19 V.

increases correspondingly. For Fig. 17(c), when the injection frequency is raised to 150 Hz, the position estimation error is -2.9°. For higher frequencies, the mutual inductance becomes the dominant factor affecting position estimation.

To further evaluate the dynamic performance of the proposed method at different speeds, Fig. 18 shows the experiment results of sudden addition and reduction of 100% rated load at 0 r/min and 100 r/min. From Fig. 18(a), the maximum speed estimation error is 26 r/min, and it takes 0.6 s to reach steady state. From Fig. 18(b), the proposed method also achieves stable operation during load variation at 100 r/min. The maximum speed estimation error is 32 r/min, and the settling time is 0.6 s. Moreover, from Fig. 18, the position estimation errors exist under no load, about 9.1° at 0 r/min and 9.4° at 100 r/min. Since this method accounts for both the stator resistance and the mutual inductance, the position error can be reduced under heavy load. However, the mutual inductance is approximately zero under no load, so the stator resistance dominates and produces a relatively larger residual error. For comparison, the conventional method exhibits a position error of about 42.1° under heavy load and an even larger error under no load, which indicates superior performance of the proposed method.

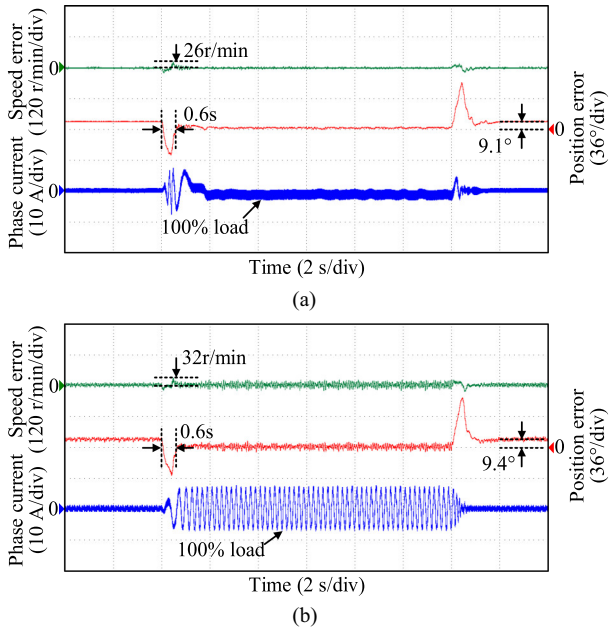

Fig. 18. Experimental results under load variation conditions. (a) 0 r/min. (b) 100 r/min.

Fig. 19 shows the experimental results of different injection methods under motor parameter variations at 100 r/min and rated load. The injection frequency is 80 Hz for all three methods. Fig. 19(a) shows the results of the LF voltage injection method. Since the excited current is computed from motor parameters, the position error changes with inductance variations and exhibits larger fluctuations than the other two methods. Fig. 19(b) shows the results of the LF current injection method. During inductance variations, the position error remains around -19.1°, and only the fluctuation magnitude changes. Since the rotor saliency introduces an additional disturbance for this method, a position error exists [27]. Fig. 19(c) shows the results of the proposed method. The position error is essentially unchanged under inductance variations. These results indicate superior position estimation performance of the proposed method.

A comprehensive comparison of the computation burden for the three methods is presented in Fig. 20. The proposed method requires an execution time of 15.94 μs, compared to 10.89 μs for the LF voltage injection method [17] and 12.84 μs for the LF current injection method [18]. Although the proposed method involves a higher computational load than the other two methods, the position estimation performance is improved. Moreover, the proposed method takes up 9.6% of the interruption time at the switching frequency of 6 kHz, and the increased computation time is acceptable for most microprocessors.

Fig. 21 shows the experimental results of startup from zero speed under rated load. The speed is first held at 0 r/min while 100% rated load is applied, then the motor accelerates from 0 to 100 r/min under 100% rated load. During the loaded startup, the maximum position estimation error is -15.1° at the start instant. After the speed reaches 100 r/min, the error decreases to 2.2°. These results indicate that the proposed method can achieve a stable startup under rated load.

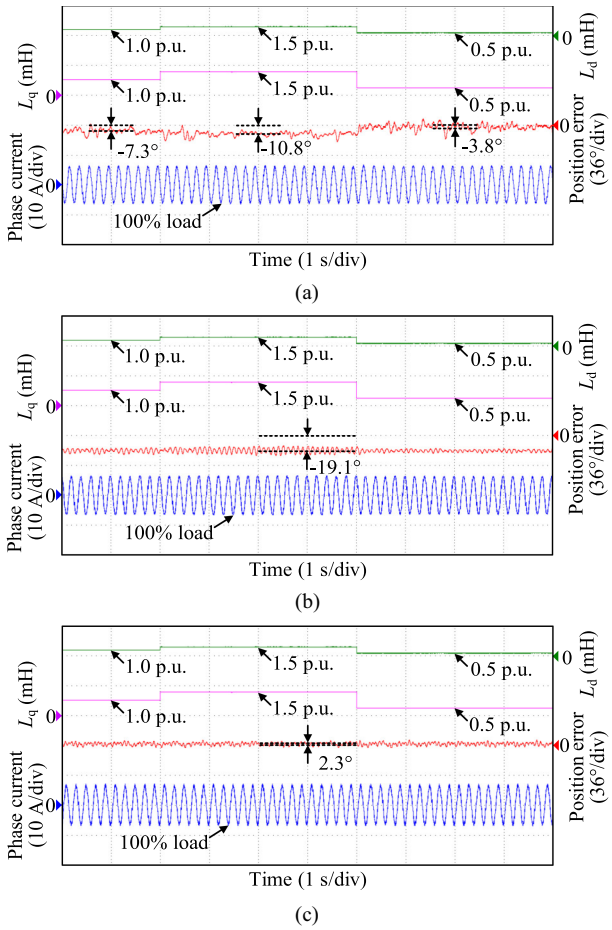

Fig. 19. Comparative experimental results of different injection methods under motor parameter variations. (a) LF voltage injection method [17]. (b) LF current injection method [18]. (c) Proposed method.

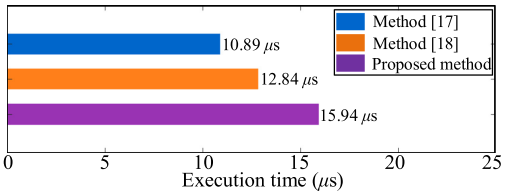

Fig. 20. Comparison of execution times for different methods.

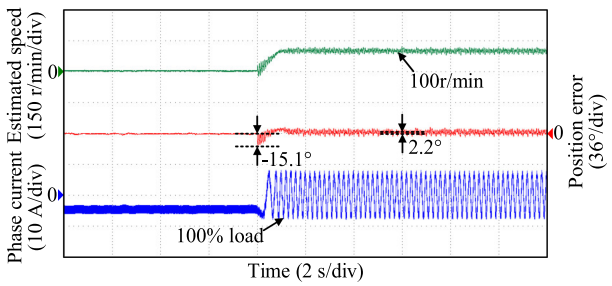

Fig. 21. Experimental results of startup from zero speed under rated load.

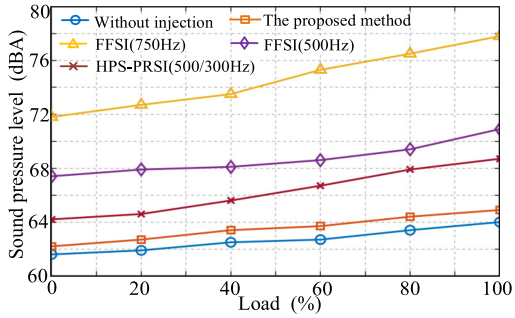

Fig. 22. Experimental sound level comparison for different injection strategies.

To further validate the effectiveness of the proposed acoustic noise reduction strategy, Fig. 22 compares the sound level for FFSI, HPS-PRSI [16], sensored control without injection, and the proposed method. It is noted that the acoustic noise is still evident in the experimental results without injection, which originates from inherent sources like harmonic torque caused by back-EMF harmonics, mechanical bearing noise, and the drive's cooling fans. The load is increased from 0 to 100% rated load in 20% steps. As shown in Fig. 22, the proposed method yields markedly lower sound levels than FFSI and HPS-PRSI, approaching the no-injection case. Moreover, a fixed frequency of 500 Hz produces a lower sound level than 750 Hz for FFSI, indicating that reducing the injection frequency can lower acoustic noise. At 100% rated load, the proposed method reduces the sound level by about 12.9 dBA and 6.0 dBA relative to FFSI at 750 Hz and 500 Hz, respectively, and by 3.8 dBA relative to HPS-PRSI at 500/300 Hz. Therefore, the proposed method can reduce acoustic noise by lowering the injection frequency to 80 Hz.

V. Conclusion

In this article, a PNSC decoupling and reconstruction-based position estimation method using the LF injection method has been proposed, which effectively reduces acoustic noise. The CD-CCF was designed to separate the fundamental currents and the LF excited currents without phase shift, eliminating the position estimation error introduced by the conventional BPF/HPF-based demodulation. A PNSC reconstruction-based error suppression strategy was proposed to reduce the estimation error caused by the stator resistance and mutual inductance. Furthermore, a unified mapping between the injection frequency and the position estimation error was established, which enables frequency optimization and further reduces estimation error. Compared with the LF voltage injection method, the proposed method reduces dependence on motor parameters. Compared with the LF current injection method, the proposed method avoids the impact of the rotor saliency on position estimation. In terms of noise reduction, the proposed method lowers acoustic noise by 6.0 dBA relative to FFSI at 500 Hz and by 3.8 dBA relative to HPS-PRSI at 500/300 Hz at 100% rated load. The experimental results show that the proposed method can effectively reduce acoustic noise and exhibit parameter robustness.

REFERENCES

[1] Z. Novak and M. Novak, "Adaptive PLL-based sensorless control for improved dynamics of high-speed PMSM," *IEEE Trans. Power Electron.*, vol. 37, no. 9, pp. 10154–10165, Sep. 2022.

[2] Y. Xu, C. Lin, and J. Xing, "Transient response characteristics improvement of permanent magnet synchronous motor based on enhanced linear active disturbance rejection sensorless control," *IEEE Trans. Power Electron.*, vol. 38, no. 4, pp. 4378–4390, Apr. 2023.

[3] Y. Zuo, C. Lai, and K. L. V. Iyer, "A review of sliding mode observer based sensorless control methods for PMSM drive," *IEEE Trans. Power Electron.*, vol. 38, no. 9, pp. 11352–11367, Sep. 2023.

[4] K. Wang et al., "Zero-speed sensorless control method for IPMSM drives using virtual voltage signal injection based full-order state observer," *IEEE Trans. Power Electron.*, vol. 40, no. 9, pp. 12428–12439, Sep. 2025.

[5] L. Guo, W. Xu, N. Jin, and H. Xiao, "A DC-offset removed sensorless control method for PMSM based on SMO with an improved prefilter and a speed immune position error compensation strategy," *IEEE Trans. Power Electron.*, vol. 40, no. 4, pp. 5163–5176, Apr. 2025.

[6] A. T. Woldegiorgis, X. Ge, H. Wang, and Y. Zuo, "An active flux estimation in the estimated reference frame for sensorless control of IPMSM," *IEEE Trans. Power Electron.*, vol. 37, no. 8, pp. 9047–9060, Aug. 2022.

[7] K. Yu, S. Li, W. Zhu, and Z. Wang, "Sensorless control scheme for PMSM drive via generalized proportional integral observers and Kalman filter," *IEEE Trans. Power Electron.*, vol. 40, no. 3, pp. 4020–4033, Mar. 2025.

[8] X. Sun, F. Cai, Z. Yang, and X. Tian, "Finite position control of interior permanent magnet synchronous motors at low speed," *IEEE Trans. Power Electron.*, vol. 37, no. 7, pp. 7729–7738, Jul. 2022.

[9] Z. Mai et al., "HF pulsating carrier voltage injection method based on improved position error signal extraction strategy for PMSM position sensorless control," *IEEE Trans. Power Electron.*, vol. 36, no. 8, pp. 9348–9360, Aug. 2021.

[10] Z. Wang, C. Gao, M. Gu, and M. Cheng, "A novel vector magnetic circuit based position observer for IPMSM drives using high-frequency signal injection," *IEEE Trans. Power Electron.*, vol. 39, no. 1, pp. 1333–1342, Jan. 2024.

[11] A. Benevieri, A. Formentini, M. Marchesoni, M. Passalacqua, and L. Vaccaro, "Sensorless control with switching frequency square wave voltage injection for SPMSM with low rotor magnetic anisotropy," *IEEE Trans. Power Electron.*, vol. 38, no. 8, pp. 10060–10072, Aug. 2023.

[12] Z. Xu, J. Zhang, J. Xiong, Y. Wu, and M. Cheng, "An improved high-frequency voltage injection method for interturn short-circuit fault detection in PMSMs," *IEEE Trans. Transp. Electrific.*, vol. 9, no. 2, pp. 3228–3239, Jun. 2023.

[13] G. Wang, L. Yang, B. Yuan, B. Wang, G. Zhang, and D. Xu, "Pseudo-random high-frequency square-wave voltage injection based sensorless control of IPMSM drives for audible noise reduction," *IEEE Trans. Ind. Electron.*, vol. 63, no. 12, pp. 7423–7433, Dec. 2016.

[14] G. Zhang et al., "Hybrid pseudorandom signal injection for position sensorless SynRM drives with acoustic noise reduction," *IEEE Trans. Transp. Electrific.*, vol. 8, no. 1, pp. 1313–1325, Mar. 2022.

[15] J. Chen, Y. Fan, W. Wang, C. H. T. Lee, and Y. Wang, "Sensorless control for SynRM drives using a pseudo-random high-frequency triangular-wave current signal injection scheme," *IEEE Trans. Power Electron.*, vol. 37, no. 6, pp. 7122–7131, Jun. 2022.

[16] G. Zhang, S. Li, B. Li, Q. Wang, G. Wang, and D. Xu, "Acoustic noise reduction using half-period-switching pseudorandom sinusoidal injection with external tangent demodulation for sensorless PMSM drives," *IEEE Trans. Transp. Electrific.*, vol. 11, no. 2, pp. 5312–5323, Apr. 2025.

[17] R. Brugioni, E. Carfagna, E. Lorenzani, and F. Immovilli, "Critical aspects and strategies for sensorless control of IPMSM based on low-frequency voltage injection," in *Proc. IEEE 10th Int. Symp. Sensorless Control Elect. Drives*, 2019, pp. 1–6.

[18] T. He and J. Chu, "Adaptive observer enhanced with low-frequency signal injection for sensorless control of PMSM," in *Proc. 22nd Int. Conf. Elect. Mach. Syst.*, 2019, pp. 1–5.

[19] G. Wang, D. Xiao, N. Zhao, X. Zhang, W. Wang, and D. Xu, "Low-frequency pulse voltage injection scheme-based sensorless control of IPMSM drives for audible noise reduction," *IEEE Trans. Ind. Electron.*, vol. 64, no. 11, pp. 8415–8426, Nov. 2017.

[20] D. Luo, H. Ji, Z. Chen, X. Wang, and D. Xiao, "Audible noise and EMI mitigation in IPMSM zero or low-speed sensorless drive with randomized low-frequency pulse voltage injection," *IEEE Trans. Transp. Electrific.*, vol. 11, no. 1, pp. 2425–2434, Feb. 2025.

[21] P. Chen, R. Ma, H. Bai, S. Song, and Z. Chen, "The impact of stator resistance on initial rotor position detection for PMSM using high frequency voltage injection," *IEEE Trans. Transp. Electrific.*, vol. 11, no. 4, pp. 9580–9589, Aug. 2025.

[22] Q. Tang, A. Shen, X. Luo, and J. Xu, "IPMSM sensorless control by injecting bidirectional rotating HF carrier signals," *IEEE Trans. Power Electron.*, vol. 33, no. 12, pp. 10698–10707, Dec. 2018.

[23] M. Naderian, G. A. Markadeh, M. Karimi-Ghartemani, and M. Mojiri, "Improved sensorless control strategy for IPMSM using an ePLL approach with high-frequency injection," *IEEE Trans. Ind. Electron.*, vol. 71, no. 3, pp. 2231–2241, Mar. 2024.

[24] P. Chen, R. Ma, H. Bai, Z. Chen, and S. Song, "DSOGI-based time delay suppression for sensorless control of SPMSM using pulsating high-frequency voltage injection," *IEEE Trans. Transp. Electrific.*, vol. 11, no. 2, pp. 6154–6164, Apr. 2025.

[25] X. K. Xie, "Stable polynomials with complex coefficients," in *Proc. 24th IEEE Conf. Decis. Control*, 1985, pp. 324–325.

[26] H. Bao and I. M. S. Panahi, "Using a-weighting for psychoacoustic active noise control," in *Proc. Annu. Int. Conf. IEEE Eng. Med. Biol. Soc.*, 2009, pp. 5701–5704.

[27] M. Eskola and H. Tuusa, "Sensorless control of salient pole PMSM using a low-frequency signal injection," in *Proc. Eur. Conf. Power Electron. Appl.*, 2005, pp. 1–10.

Yunhao Yan received the B.S. degree in electrical engineering from the Harbin Institute of Technology, Harbin, China, in 2023, where he is currently working toward the Ph.D. degree in electrical engineering with the School of Electrical Engineering and Automation. His research interests include sensorless control of permanent magnet synchronous motor drives and maximum torque per ampere (MTPA) control.

Guoqiang Zhang (Senior Member, IEEE) received the B.S. degree in electrical engineering from Harbin Engineering University, Harbin, China, in 2011, and the M.S. and Ph.D. degrees in electrical engineering from Harbin Institute of Technology, Harbin, China, in 2013 and 2017, respectively. Since 2017, he has been with the Department of Electrical Engineering, Harbin Institute of Technology, where he is currently a Professor. His research interests include control of electrical drives and parameter identification techniques, with a main focus on sensorless field-oriented control of synchronous motor drives. Dr. Zhang is currently an Associate Editor for IEEE TRANSACTIONS ON ENERGY CONVERSION.

Gaolin Wang (Senior Member, IEEE) received the B.S., M.S., and Ph.D. degrees in electrical engineering from Harbin Institute of Technology, Harbin, China, in 2002, 2004, and 2008, respectively. In 2009, he joined the Department of Electrical Engineering, Harbin Institute of Technology, as a Lecturer, where he has been a Full Professor of Electrical Engineering since 2014. From 2009 to 2012, he was a Postdoctoral Fellow with Shanghai Step Electric Corporation, where he was involved in the traction machine control for direct-drive elevators. He has authored more than 70 technical papers published in IEEE transactions. He is the holder of 40 Chinese patents. His research interests include permanent magnet synchronous motor drives, position sensorless control of ac motors, and digital control of power converters. Dr. Wang is currently a Guest Associate Editor of IEEE TRANSACTIONS ON INDUSTRIAL ELECTRONICS, an Associate Editor of IEEE TRANSACTIONS ON TRANSPORTATION ELECTRIFICATION, *IET Electric Power Applications*, and JOURNAL OF POWER ELECTRONICS.

Kairan Wang received the B.S. degree in electrical engineering in 2022 from Harbin Institute of Technology, Harbin, China, where he is currently working toward the Ph.D. degree in power electronics and electrical drives. His research interests include permanent magnet synchronous motor drives and PMa-SynRM position sensorless control.

Binxing Li (Member, IEEE) received the B.S. degree in electrical engineering from Harbin Institute of Technology (HIT), Weihai, China, in 2017, and the Ph.D. degree in electrical engineering from HIT, Harbin, China, in 2022. He is currently a Postdoctoral Student with the School of Electrical Engineering and Automation, HIT. His current research interests include permanent magnet synchronous motor drives, high-efficiency ac–dc converters, and the application of GaN power devices.

Qiwei Wang (Member, IEEE) received the B.S., M.S., and Ph.D. degrees in electrical engineering from the Harbin Institute of Technology, Harbin, China, in 2015, 2017, and 2022, respectively. He is currently an Associate Professor in power electronics and electrical drives with the School of Electrical Engineering and Automation, Harbin Institute of Technology. His research interests include parameter identification techniques and permanent magnet synchronous motor position sensorless control.

Dawei Ding (Member, IEEE) received the B.S. and M.S. degrees in electrical engineering from Hefei University of Technology, Hefei, China, in 2014 and 2017, respectively, and the Ph.D. degree in electrical engineering from Harbin Institute of Technology (HIT), in 2021. He is currently an Associate Professor with the School of Electrical Engineering and Automation, HIT. From 2020 to 2021, he was a visiting Ph.D. student with Technical University of Denmark. He has authored more than 50 journal papers in IEEE transactions and holds tens of authorized Chinese invention patents. His research interests include advanced control of permanent magnet synchronous motor drives and electrolytic capacitorless ac motor drives.

Dianguo Xu (Fellow, IEEE) received the B.S. degree in control engineering from Harbin Engineering University, Harbin, China, in 1982, and the M.S. and Ph.D. degrees in electrical engineering from Harbin Institute of Technology (HIT), Harbin, China, in 1984 and 1989, respectively. In 1984, he joined the Department of Electrical Engineering, HIT, as an Assistant Professor. Since 1994, he has been a Professor with the Department of Electrical Engineering, HIT. He was the Dean of the School of Electrical Engineering and Automation, HIT, from 2000 to 2010, and the Assistant President from 2010 to 2014. He is currently the Vice President of the HIT. He authored or coauthored more than 600 technical papers. His research interests include renewable energy generation technology, power quality mitigation, sensorless vector-controlled motor drives, and high-performance permanent magnet synchronous motor servo systems. Dr. Xu is the Co-EIC of IEEE TRANSACTIONS ON POWER ELECTRONICS, an Associate Editor of IEEE TRANSACTIONS ON INDUSTRIAL ELECTRONICS, and IEEE JOURNAL OF EMERGING AND SELECTED TOPICS IN POWER ELECTRONICS. He was the recipient of the 2018 IEEE IAS Outstanding Achievement Award.